Robotica (2016) volume 34, pp. 361–382. © Cambridge University Press 2014
doi:10.1017/S0263574714001507

Performance analysis and parameter optimization of an inner spiral in-pipe robot

Liang Liang†*, Hui Peng‡, Bai Chen§, Yong Tang†, Sun Chen¶ and Yan Xu†

†*Department of Mechanical & Electrical Engineering, Changsha University, Changsha 410022, China*
‡*College of Information Science and Engineering, Central South University, Changsha 410083, China*
§*Jiangsu Key Laboratory of Precision and Micro-Manufacturing Technology, Nanjing University of Aeronautics and Astronautics, Nanjing 210016, China*
¶*Xin Hua Hospital Affiliated to Shanghai Jiao Tong University School of Medicine, Shanghai 200092, China*

(Accepted May 19, 2014. First published online: June 20, 2014)

SUMMARY
A novel micro in-pipe robot using an internally threaded profile for propulsion is proposed in this paper, and the dynamic model of the robot in the turbulent liquid pipeline is established, and the computational fluid dynamics method is used to solve the influence of environmental parameters and operating parameters on the robotic performance. By the orthogonal experimental optimization method, the optimal inner spiral structural parametrical combination is obtained. According to the working principle of the inner spiral robot, an inner spiral driving device is designed and fabricated, and the running experiment in the pipeline full of 201 methyl silicone oil verifies the feasibility of the proposed robot. Adopting the pulsating blood flow function as the inlet condition, in a pulsating period, the robotic performance is numerically analyzed.

KEYWORDS: Computational fluid dynamics; Inner spiral in-pipe robots; Orthogonal optimization; Pulsating blood flow.

1. Introduction

There are many small-diameter pipelines filled with liquid in human body, such as gastrointestinal tracts, blood vessels, etc. The basic operation of inspection and sampling in the human pipelines adopts the traditional way such as directly inserting endoscopic catheters. As the catheters are inserted by human hands, they can easily damage soft tissues and cause pain to a patient. Especially when the effective inserting length of the catheter is great and the curved shape of the catheter is complex, the endoscope is difficult to go deep into the corners inside the human body, and it is often difficult to achieve effective diagnoses and treatments. To solve these problems, scientists began to seek appropriate improving ways to make up for the above defects. In recent years, the medical micro system inside human body has emerged as the times required. To develop autonomous medical micro robots for placing into the human pipelines to complete the minimally invasive or noninvasive diagnoses and treatments has become a hot research topic in the field of international medical and electronic field.

Since 1999, some medical capsule endoscope systems have been developed,[1–4] which end the discomfort and the problems that the traditional medical endoscopic catheter insertion brings. The wireless capsule endoscope system mainly relies on the gastrointestinal motility to achieve its own

* Corresponding author. E-mail: fatliangliang@126.com
E-mails: huipeng@csu.edu.cn, chenbye@126.com, tytss@126.com, chengsun@hotmail.com, x_y616@163.com

https://doi.org/10.1017/S0263574714001507 Published online by Cambridge University Press

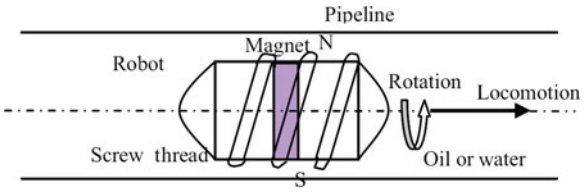


Fig. 1. A single-sectional outer spiral-type in-pipe robot.[16]

motion. The system cannot control its moving speed and determine its position. The system also cannot seriously and carefully check a certain position, and therefore it's potential to cause the omission. The moving direction of the system is not changed, so the diseased region is not effectively treated. Thus the active capsule in-pipe robots appear. The leg type of capsule endoscopic robots have all been developed,[5,6] which use micro battery or external magnetic field to actuate, and their movement mode is peristalsis. Peristalsis refers to crawling such as insects' creeping, and it is a typical mode of soft animal movement; for example inchworms, earthworms, and snakes move by peristalsis. Various crawling bionic in-pipe robots have all been developed.[7–10] The researchers do not intensively study inchworm-like or earthworm-like or snake-like, and they research for different actuating materials, for different robot design schemes corresponding to different actuators. Actuating materials include shape memory alloys, ion-exchange polymer metal composite, piezoelectric materials, ionic conducting polymer films, and so on. When the crawling in-pipe robots are running, the robots contact directly with the pipeline walls, which easily damage the inner walls; especially when they are pipelines of human body, the robots cause some damage to the inner organic tissues of the body and result in human suffering and discomfort.

A large number of animal species live in water, and their movement mode is swimming. Water is the medium of aquatic animal movement, and it is much heavier than air. An aquatic animal is subject to the buoyancy of water, and the resistance to its movement in the water is larger than that in the air. Some fish-like, jellyfish-like, sperm-like, and tadpole-like swimming in-pipe robots have been developed.[11–14] The swimming robots are flexible, and their acceleration performance is good. However, their backward movements need large-angle steering. When the diameter of the operating pipeline is small, such as blood vessels, the large-scale steering of the robot is basically difficult to achieve; therefore, for the swimming robots, their backward movement and position adjustment are main problems.

Ikeuchi found that in a pipeline filled with fluid, when a cylinder with a spiral shell rotates at a high speed, the liquid produces axial thrust on the cylinder.[15] When liquid has a certain viscosity, it produces supporting force along the opposite direction of gravity because of the dynamic pressure effect of liquid. And then a layer of liquid membrane which separates the cylinder from the pipeline wall is formed. Therefore, the spiral-type robot is a novel in-pipe robot that causes relatively less damage to the pipeline. A single sectional spiral-type micro in-pipe robot is driven by external magnetic field in the pipeline filled with fluid, as shown in Fig. 1.[16] Controlling the strength and direction of the external magnetic field can change the clockwise or counterclockwise rotation of the permanent magnet inside the robot, so the produced liquid force drives the robot forward or backward. Zhou Yinsheng proposed a double-sectional spiral-type medical micro in-pipe robot, as shown in Fig. 2.[17] The robot consists of a cylinder with a left spiral groove, a micro motor with a right spiral shell, and a flexible coupling. When the power of the micro motor is turned on, the rotational direction of the micro motor with the right spiral shell is opposite to that of the cylinder with the left spiral shell, and the two thrust forces generated by the fluid have the same directions. Changing the rotational direction of the micro motor can change the moving direction of the robot. The flexible coupling can make the robot move in a bent pipeline.

The above-mentioned spiral robots use spiral grooves or spiral strips on the outer surface. When the robots rotate at a high speed, the thrust of liquid to the robotic surface drives the robot to move. At the same time, according to the dynamic pressure effect of the liquid in the pipeline, the supporting force of the robot is produced, and a liquid film is formed, which can help to avoid damage to the inner wall of the pipeline. But when the liquid film's thickness is small and the rotating speed of the robot is high, the robotic spiral shell may cause damage to the inner wall of the pipeline. At the

https://doi.org/10.1017/S0263574714001507 Published online by Cambridge University Press

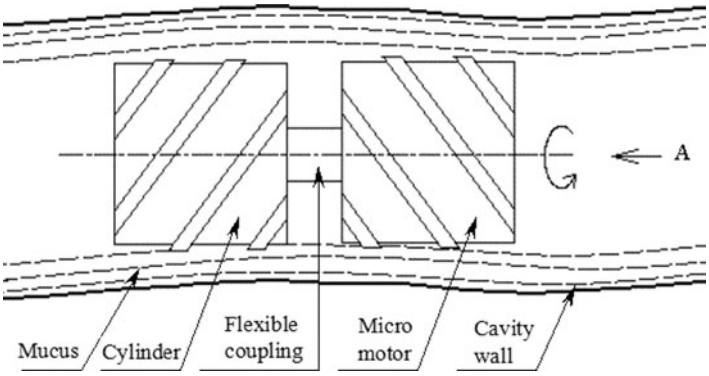


Fig. 2. A double sectional outer spiral-type in-pipe robot.[17]

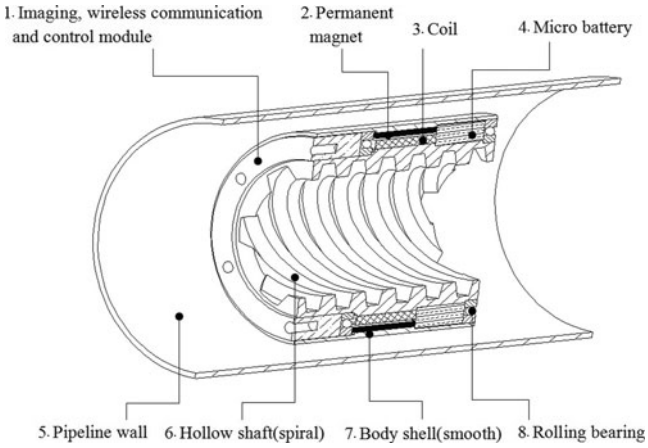


Fig. 3. Structural diagram of the inner spiral in-pipe robot.

same time, when the rotating speed of the robot shell is reduced, the supporting force formed by the dynamic pressure effect of the liquid is not enough to support the robot, thus the robot will contact the inner wall of the pipeline and damage it.

Aiming to overcome the above problems of the outer spiral in-pipe robots, a novel inner spiral in-pipe robot with smooth surface is proposed based on liquid environment. The dynamic model of the robot in the liquid pipeline is established, and the correctness of the adopted numerical method is verified, and the influences of environmental parameters and operating parameters on the performance of the robot are researched, and the structural parameters of the robot are optimized, and the experiment verifies the working principle of the robot. In the end, the operation of the robot in the pulsating flow field is analyzed. The proposed robots are expected to be applied to gastrointestinal tracts, blood vessels, and other tiny pipelines filled with liquid, conducting inspection, sampling, dredging, and other functions.

2. Structural Design of the Inner Spiral Robot

Based on the outer spiral micro in-pipe robots showed in Figs. 1 and 2, the authors propose an inner spiral micro in-pipe robot in liquid environment. This robot is small in size, and its outer surface is smooth, and it is less invasive, and the rotational speeds of its inner and outer surfaces are changeable.

The structure of the inner spiral robot is shown in Fig. 3. In Fig. 3, the permanent magnet 2 and the coil 3 compose of the micro motor, between which the rolling (or sliding) bearing 8 supports. The permanent magnet 2 is fixed on the smooth body shell 7, and the coil 3 is fixed on the hollow shaft 6 with left threads. The micro battery 4 and other modules are fixed on the hollow shaft 6 or the smooth body shell 7. At the beginning, because the robotic outer shell is in contact with the pipeline wall 5, there is a frictional force. When the power is turned on, the inner spiral portion of the robot rotates, and the liquid within the hollow shaft will produce axial thrust force and supporting force.

https://doi.org/10.1017/S0263574714001507 Published online by Cambridge University Press

Meanwhile, the liquid resistance is generated, which hinders the inner spiral portion to rotate, and the outer shell begins to rotate. According to Newton's third law, the torque given to hollow shaft 6 equals the torque given to body shell 7. Since 6 and 7 are not fixed, and the surface area of 7 is greater than that of 6, that is, liquid resistance of 7 is greater than that of 6 under the same rotational speeds, the rotational speed of 6 is greater than that of 7 under actual condition. The robotic inner and outer axial thrust forces decrease with the increase of the robotic running speed, and when the robotic axial thrust force is equal to 0, at this time, the robot runs at a constant speed. Adjusting the area ratio between the body shell part and the hollow shaft part can change the rotational speeds of the inner and outer surfaces of the robot.

Due to the dynamic pressure effect of liquid, a layer of liquid film will be formed between the robot shell and the working pipeline wall 5, and the robot is in a suspended state, which avoids the direct contact between the robot and the pipeline wall, so as to achieve the purpose of driving without injury. Changing the rotational direction of the micro motor can change the direction of the robotic thrust force, that is, change the direction of the robotic motion. The imaging, wireless communication, and control module 1 are also arranged along the robotic body circumference, and the wireless control of the robot can be achieved.

3. Dynamic Equation of the Liquid in the Pipeline

When the proposed spiral robot runs in the pipeline full of liquid, the liquid in the pipeline also flows. Through the analysis of the liquid flow field near the robot (pressure field and velocity field), the robotic force and velocity can be gotten. To analyze the flow field of the liquid in the pipeline, the dynamic equation of the liquid is first established.

Turbulent flow is very common in nature. In the turbulent motion process, the fluid particles mix and move randomly. The local velocity, pressure, and other physical quantities are likely to pulsate irregularly in space and time. When the spiral in-pipe robot rotates at high speed in the pipeline full of liquid, the liquid flow is turbulent flow. The pressure and velocity of the liquid vary with time, and the pulsation is strong. Suppose the liquid is the Newton fluid, and it is not affected by temperature and pressure, and the inner and outer surfaces of the robot are rigid.

The fluid continuity equation and momentum equation are:[18]

$$\frac{\partial}{\partial x_i}(\rho u_i) = 0 \quad (i = 1, 2, 3), \tag{1}$$

$$\frac{\partial(\rho u_i)}{\partial t} + \frac{\partial(\rho u_i u_j)}{\partial x_j} = -\frac{\partial p}{\partial x_i} + \frac{\partial}{\partial x_j}\left(\mu \frac{\partial u_i}{\partial x_j} - \rho\overline{u_i' u_j'}\right) + F_i, \tag{2}$$

where t is time, x_i is Cartesian coordinate, u_i is fluid velocity mean of the x_i direction, u_i' is fluid velocity pulsate value of the x_i direction, p is pressure time mean value on the fluid micro unit, ρ is density of the fluid, μ is fluidic dynamic viscosity, and F_i is physical strength on the fluid micro unit.

The eddy viscosity model of the Reynolds averaging method is adopted as the turbulent model, and it can be written as

$$-\rho\overline{u_i' u_j'} = \mu_t\left(\frac{\partial u_i}{\partial x_j} + \frac{\partial u_j}{\partial x_i}\right) - \frac{2}{3}\left(\rho k + \mu_t \frac{\partial u_i}{\partial x_i}\right)\delta_{ij},$$
$$\text{among } \delta_{ij} = \begin{cases} 1 & i = j \\ 0 & i \neq j \end{cases}, \tag{3}$$

where μ_t is turbulent viscosity, and k is turbulent kinetic energy.

Eddy viscosity model adopts the standard k–ε turbulent model, where ε is turbulent dissipation rate. Turbulent viscosity μ_t can be expressed as a function of k and ε, i.e.

$$\mu_t = \rho C_\mu \frac{k^2}{\varepsilon}, \tag{4}$$

where C_μ is an empirical constant and is 0.09.

https://doi.org/10.1017/S0263574714001507 Published online by Cambridge University Press

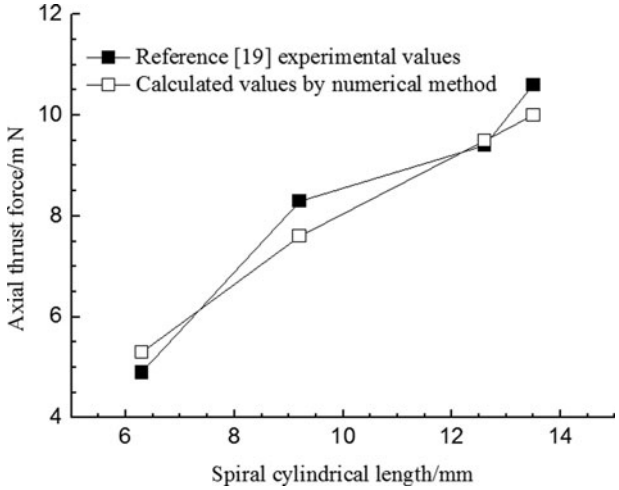


Fig. 4. Variation curve of the axial thrust force with the rotational cylindrical length.

For the standard k–ε model, according to ref. [18],

$$\frac{\partial(\rho k)}{\partial t} + \frac{\partial(\rho k u_i)}{\partial x_i} = \frac{\partial}{\partial x_j}\left[\left(\mu + \frac{\mu_t}{\sigma_k}\right)\frac{\partial k}{\partial x_j}\right] + G_k - \rho\varepsilon, \tag{5}$$

$$\frac{\partial(\rho \varepsilon)}{\partial t} + \frac{\partial(\rho \varepsilon u_i)}{\partial x_i} = \frac{\partial}{\partial x_j}\left[\left(\mu + \frac{\mu_t}{\sigma_\varepsilon}\right)\frac{\partial \varepsilon}{\partial x_j}\right] + \frac{C_{1\varepsilon}\varepsilon}{k}G_k - C_{2\varepsilon}\rho\frac{\varepsilon^2}{k}, \tag{6}$$

$$\text{among } G_k = \mu_t\left(\frac{\partial u_i}{\partial x_j} + \frac{\partial u_j}{\partial x_i}\right)\frac{\partial u_i}{\partial x_j}, \quad \sigma_k = 1.0, \quad \sigma_\varepsilon = 1.3, \quad C_{1\varepsilon} = 1.44, \quad C_{2\varepsilon} = 1.92.$$

The above fluid continuity and momentum equations in turbulent condition are suitable for all kinds of robots in liquid environment. To obtain the analytic solution of the above partial differential equations is difficult, by using the numerical method, namely the use of computational fluid dynamics (CFD) software FLUENT 14, the approximate solution to meet the practical requirements is gotten. The steps to solve are roughly as follows. First, a three-dimensional (3D) model of the robotic system is established by using PRO/E software, and then the meshes are divided and the boundary conditions are set by GAMBIT software, and those dynamic equations are solved by the use of CFD software FLUENT. In the parameter setting, the standard k-ε turbulent model is selected. After the solution, the liquid flow field near the robot and the forces and moments on the robot are obtained.

In order to verify the correctness of the adopted numerical calculation method, the authors compute the axial thrust force of the rotational outer spiral cylindrical body with its length change in the simulating pipeline filled with silicone oil in ref. [19]. In the experiment, the viscosity of the silicone oil is 0.9 Pa s, the inner diameter of the simulating pipeline is 4.5 mm, the radius of the spiral cylindrical body is 2 mm, and its rotational speed is 800 r/min. The spiral groove is rectangular and its depth is 0.4 mm, the thread number is 6, the ratio of the groove face width to the sum of the groove face width and its bottom width is 0.5, at the same time, the central line of the spiral cylindrical body and the central line of the simulating pipeline coincide.

Figure 4 is the contrast curve of the calculated values by numerical method and the experimental values in ref. [19]. The calculated values are basically close to the experimental values, and the calculated results agree well with the experimental results, and it verifies the correctness of the numerical calculation method adopted in this paper.

4. Performance Analysis of the Robot

In the analysis of the performance of the inner spiral robot, the robot shown in Fig. 3 is applied to a pipeline filled with liquid. For practical operation, the flow of liquid in the pipeline is turbulent, and

https://doi.org/10.1017/S0263574714001507 Published online by Cambridge University Press

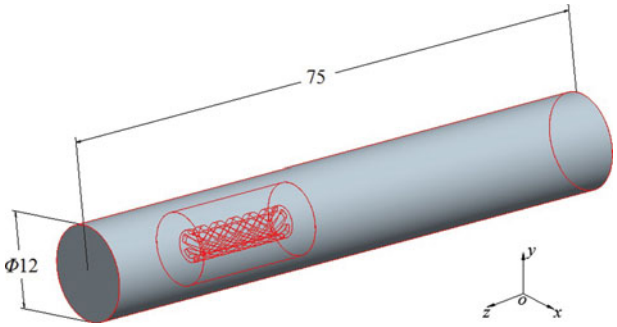


Fig. 5. The 3D diagram of the inner spiral robotic system.

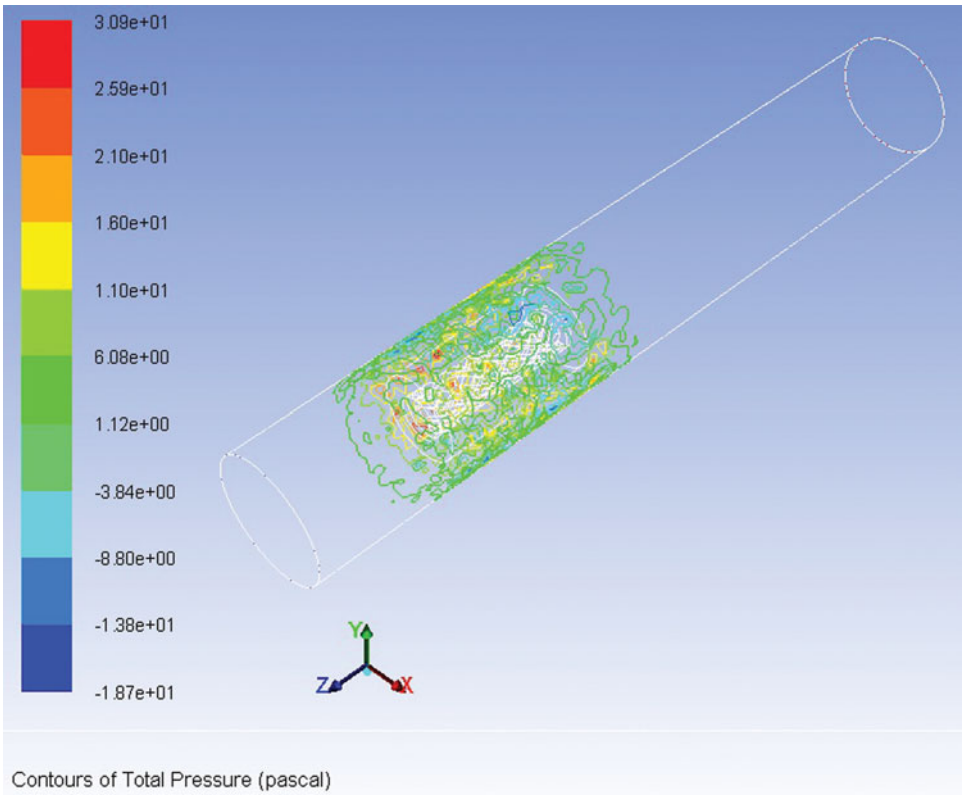


Fig. 6. Contour diagram of the pressure to the pipeline wall.

the supporting force of the liquid on the robot is equal to the weight of the robot. Here, the impact of the weight is ignored. We assume that the initial pipeline diameter is 12 mm, and the pipeline length is 75 mm. The robotic outer surface is smooth, its outer diameter is 8 mm, its axial length is 15 mm. The robotic inner spiral parameters are: inner diameter is 2.8 mm, axial length is 15 mm, thread number is 6, lead is 15 mm, spiral groove is rectangular, groove face width is 1.5 mm, groove bottom width is 1 mm, and groove depth is 0.6 mm. The robotic system is modeled by the 3D software, and the diagram is shown in Fig. 5.

In the analysis, we assume that the robotic running speed is 0, the rotational speed of the robotic shell is 600 r/min (forward), and the rotational speed of the robotic inner shaft is –600 r/min (reverse). We initially assume liquid density is 1000 kg/m^3, liquid viscosity is 1 Pa s, pipeline diameter is 12 mm, and eccentricity (the distance between the central line of the robot and the central line of the pipeline) is 0.

Figure 6 is the contour diagram of the pressure to the pipeline wall when the robot is rotating in the pipeline. Different colors represent different pressure values. As can be seen, the high-pressure area is mainly concentrated near the area around the robot, and the maximum positive pressure value

https://doi.org/10.1017/S0263574714001507 Published online by Cambridge University Press

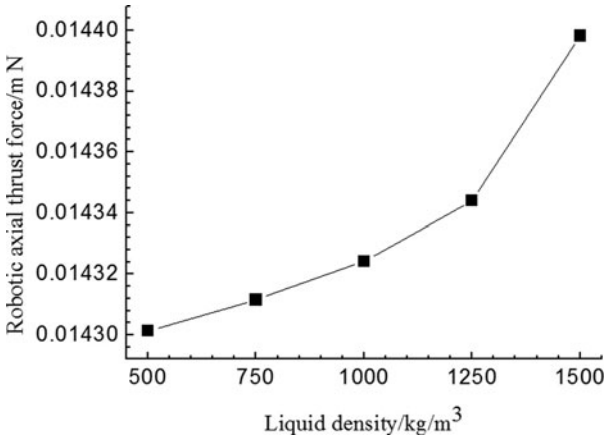


Fig. 7. Relation curve between robotic axial thrust force and liquid density.

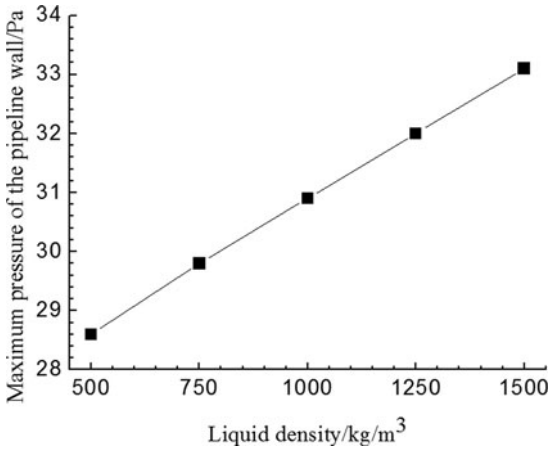


Fig. 8. Relation curve between maximum pressure of the pipeline wall and liquid density.

is 30.9 Pa, and the maximum negative pressure value is 18.7 Pa. It is showed that when the robot runs along the central axis of the pipeline, the pipeline wall is not substantially damaged.

By means of "Result Reports" of the software FLUENT 14, the robotic axial thrust force is 0.0143 m N, and the supporting force of the liquid on the robot is 0.6922 m N. When the flow of liquid is laminar, we use the same calculation method. The robotic axial thrust force is 0.0307 m N, and the supporting force of the liquid on the robot is 0.8548 m N. It shows that the liquid turbulence reduces the robotic axial thrust force and the supporting force of the liquid on the robot.

4.1. Effect of environmental parameters on the performance of the robot

When the inner spiral robot runs in the pipeline full of liquid, the environmental parameters influencing the robotic performance indexes (including the axial thrust force, the maximum pressure of the pipeline wall, and the supporting force of the liquid on the robot) involve liquid density, liquid viscosity, pipeline diameter, and eccentricity.

4.1.1. Liquid density. Liquid density changes from 500 kg/m^3 to 1500 kg/m^3. Figures 7–9 are respectively the curves of the robotic axial thrust force, the maximum pressure of the pipeline wall, and the supporting force of the liquid on the robot with liquid density. As seen here, when liquid density is increased, the robotic axial thrust force and the maximum pressure of the pipeline wall are all increased, and the supporting force of the liquid is decreased, but their changed values are smaller, which indicates the influence of liquid density on the robotic performance is smaller.

4.1.2. Liquid viscosity. Liquid viscosity changes from 0.5 Pa s to 2.5 Pa s. Figures 10–12 are respectively the curves of the robotic axial thrust force, the maximum pressure of the pipeline wall,

https://doi.org/10.1017/S0263574714001507 Published online by Cambridge University Press

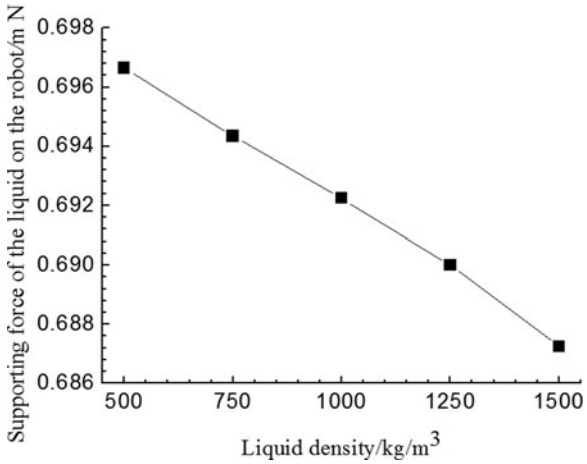


Fig. 9. Relation curve between supporting force of the liquid on the robot and liquid density.

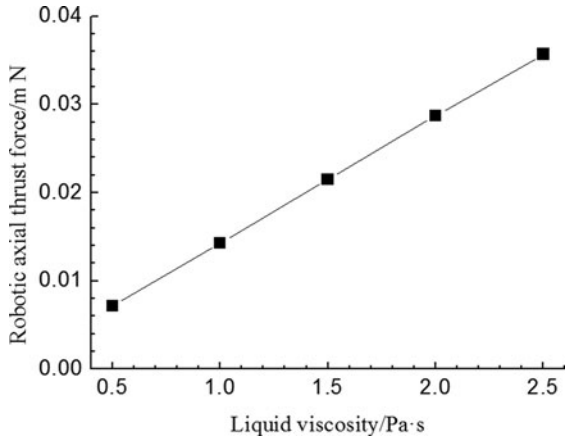


Fig. 10. Relation curve between robotic axial thrust force and liquid viscosity.

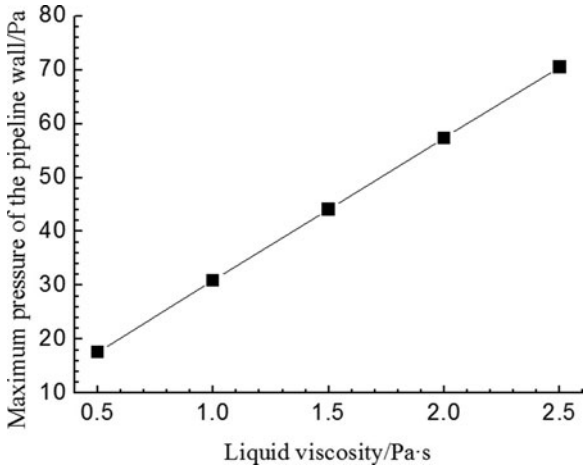


Fig. 11. Relation curve between maximum pressure of the pipeline wall and liquid viscosity.

and the supporting force of the liquid on the robot with liquid viscosity. As seen here, when liquid viscosity is increased, the robotic axial thrust force, the maximum pressure of the pipeline wall, and the supporting force of the liquid are all increased. Contrasting the influence of liquid density on the robotic performance, the influence of liquid viscosity is greater.

https://doi.org/10.1017/S0263574714001507 Published online by Cambridge University Press

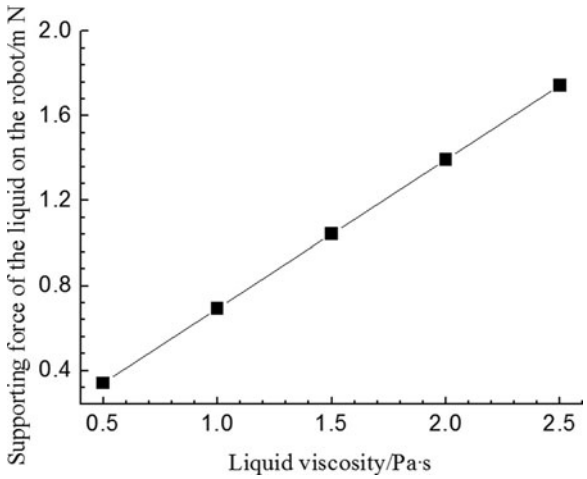


Fig. 12. Relation curve between supporting force of the liquid on the robot and liquid viscosity.

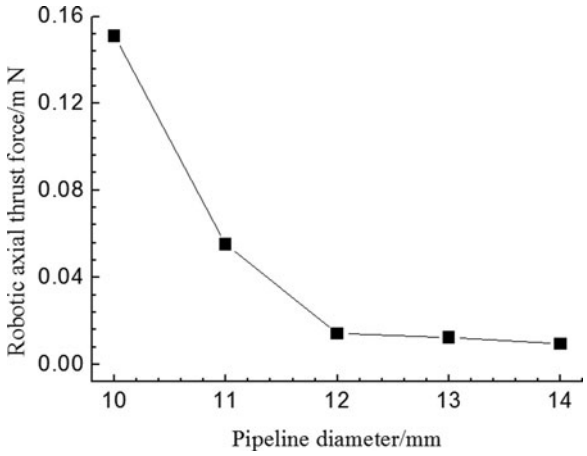


Fig. 13. Relation curve between robotic axial thrust force and pipeline diameter.

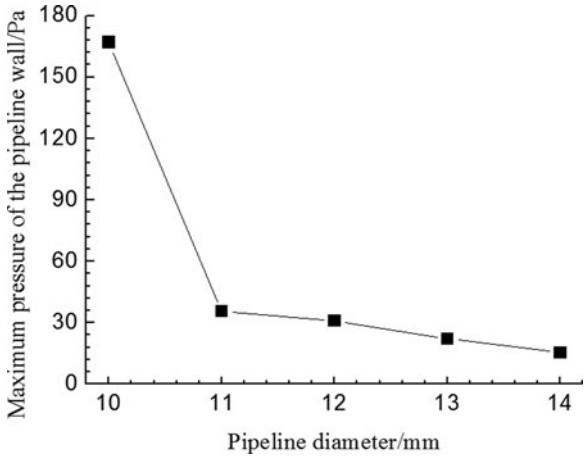


Fig. 14. Relation curve between maximum pressure of the pipeline wall and pipeline diameter.

4.1.3. Pipeline diameter. Pipeline diameter changes from 10 to 14 mm. Figures 13–15 are respectively the curves of the robotic axial thrust force, the maximum pressure of the pipeline wall, and the supporting force of the liquid on the robot with pipeline diameter. As seen here, when pipeline

https://doi.org/10.1017/S0263574714001507 Published online by Cambridge University Press

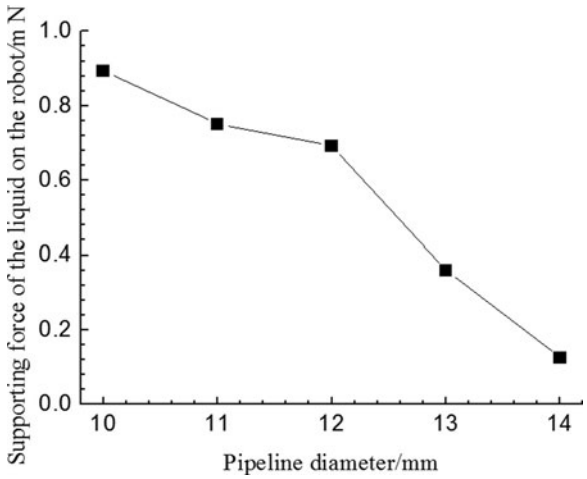


Fig. 15. Relation curve between supporting force of the liquid on the robot and pipeline diameter.

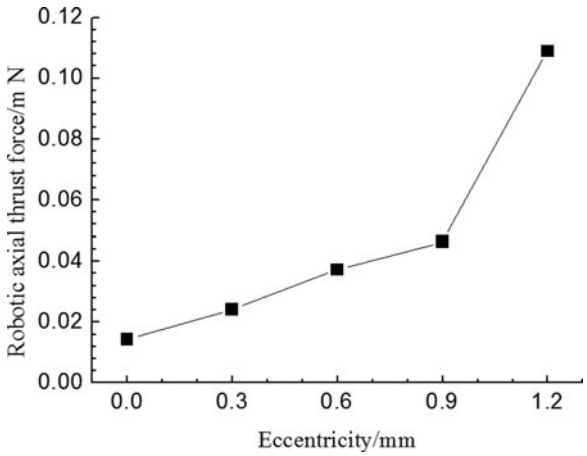


Fig. 16. Relation curve between robotic axial thrust force and eccentricity.

diameter is increased, the robotic axial thrust force, maximum pressure of the pipeline wall, and the supporting force of the liquid are all decreased, and the influence of pipeline diameter is much greater.

4.1.4. Eccentricity. Eccentricity changes from 0 to 1.2 mm. Figures 16–18 are respectively the curves of the robotic axial thrust force, the maximum pressure of the pipeline wall, and the supporting force of the liquid on the robot with eccentricity. As seen here, when eccentricity is increased, the robotic axial thrust force, the maximum pressure of the pipeline wall, and the supporting force of the liquid are all increased, and the influence of eccentricity on the robotic performance is also much greater.

4.2. Effect of operating parameters on the performance of the robot

When the inner spiral robot runs in pipeline full of liquid, the operating parameters influencing the robotic performance indexes involve inner spiral rotational speed, outer surface rotational speed, inner and outer surface rotational speed sum, robotic running speed.

In the analysis, we assume that the initial robotic running speed is 0, the initial rotational speed of the robotic shell is 600 r/min, and the initial rotational speed of the robotic inner shaft is –600 r/min. Liquid density is 1000 kg/m^3, liquid viscosity is 1 Pa s, eccentricity is 0, and pipeline diameter is 12 mm.

4.2.1. Inner spiral rotational speed and outer surface rotational speed. The rotational speed of the robotic shell changes from 200 to 1000 r/min, and the rotational speed of the robotic inner shaft changes from –200 to –1000 r/min.

https://doi.org/10.1017/S0263574714001507 Published online by Cambridge University Press

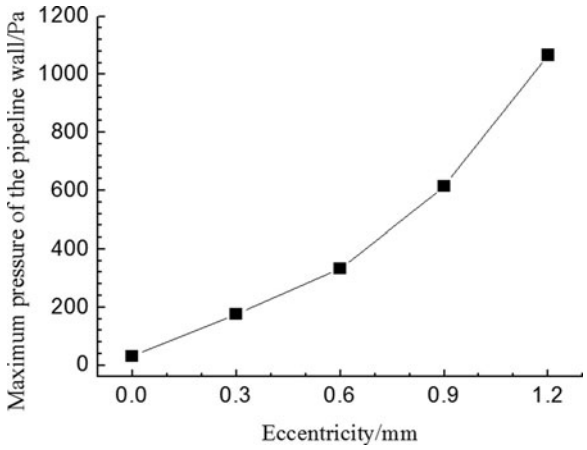


Fig. 17. Relation curve between maximum pressure of the pipeline wall and eccentricity.

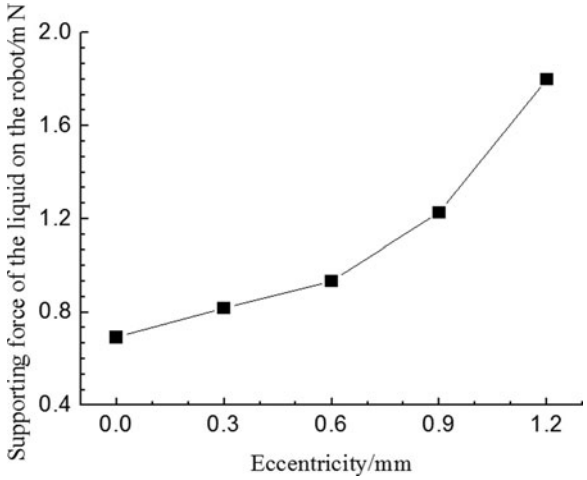


Fig. 18. Relation curve between supporting force of the liquid on the robot and eccentricity.

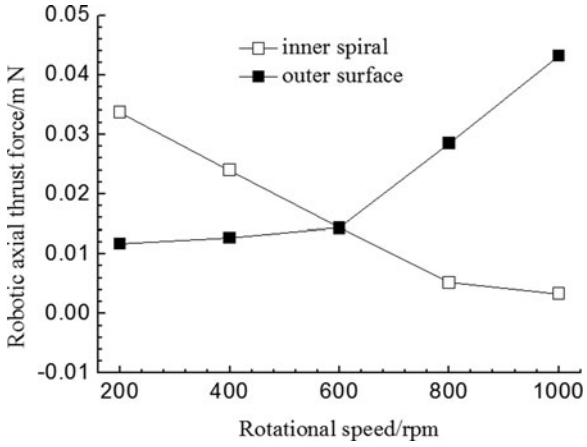


Fig. 19. Relation curve between robotic axial thrust force and inner and outer rotational speeds.

Figures 19–21 are respectively the curves of the robotic axial thrust force, the maximum pressure of the pipeline wall, and the supporting force of the liquid on the robot with inner spiral rotational speed and outer surface rotational speed.

As seen here, when outer surface rotational speed is increased, the maximum pressure of the pipeline wall and the supporting force of the liquid are increased, but when inner spiral rotational

https://doi.org/10.1017/S0263574714001507 Published online by Cambridge University Press

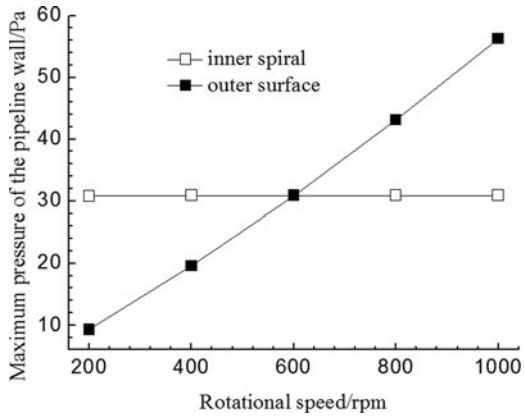


Fig. 20. Relation curve between maximum pressure of the pipeline wall and inner and outer rotational speeds.

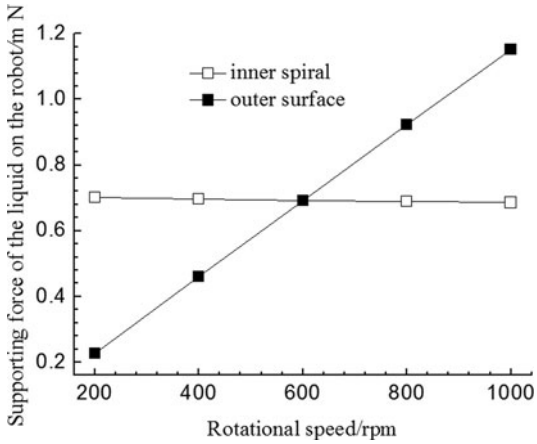


Fig. 21. Relation curve between supporting force of the liquid on the robot and inner and outer rotational speeds.

speed is increased, they do not basically change. The robotic axial thrust force is proportional to outer surface rotational speed, but it is inversely proportional to inner spiral rotational speed, and the influence of outer surface rotational speed is the same as that of the inner spiral rotational speed.

4.2.2. Inner and outer surface rotational speed sum. In actual operation, inner spiral rotational speed and outer surface rotational speed of the inner spiral robot will change each other, but their sum will remain unchanged, and it is equal to the micro motor rated speed, therefore the inner and outer surface rotational speed sum is also a very important operating parameter. We assume that the inner and outer surface rotational speed sum is constant and equals to 1200 r/min. The rotational speed of the robotic shell changes from 1000 r/min to 200 r/min, and the rotational speed of the robotic inner shaft changes from –200 to –1000 r/min. Figures 22–24 are respectively the curves of the robotic axial thrust force, the maximum pressure of the pipeline wall, and the supporting force of the liquid on the robot with inner and outer surface rotational speed sum. As seen here, although the rotational speed sum is unchanged, the robot axial thrust force, the maximum pressure of the pipeline wall, and the supporting force of the liquid are all decreased with the decrease of the outer surface rotational speed and the increase of the inner spiral rotational speed. So the influences of the outer surface rotational speed and the inner spiral rotational speed on the robotic performance are different.

4.2.3. Robotic running speed. The robotic running speeds are respectively 1 mm/s, 2 mm/s, and 3 mm/s, and the running time is 0.2 to 0.8 s for this period. Figures 25 and 26 are respectively the curves of the robotic axial thrust force and the supporting force of the liquid on the robot with robotic running speed.

As seen here, when the robot runs at a certain speed in different running times, the robotic axial thrust force and the supporting force of the liquid all change a little. When the robotic running speed is

https://doi.org/10.1017/S0263574714001507 Published online by Cambridge University Press

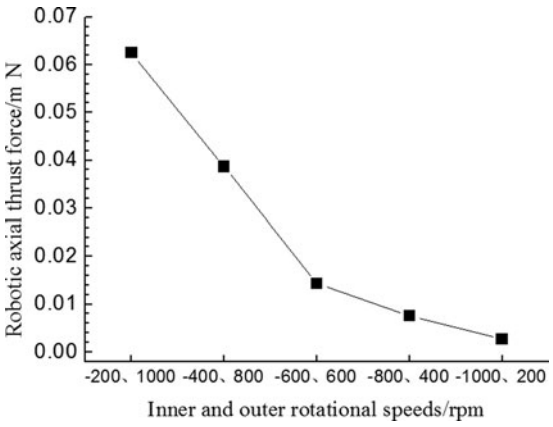


Fig. 22. Relation curve between robotic axial thrust force and inner and outer rotational speed sum.

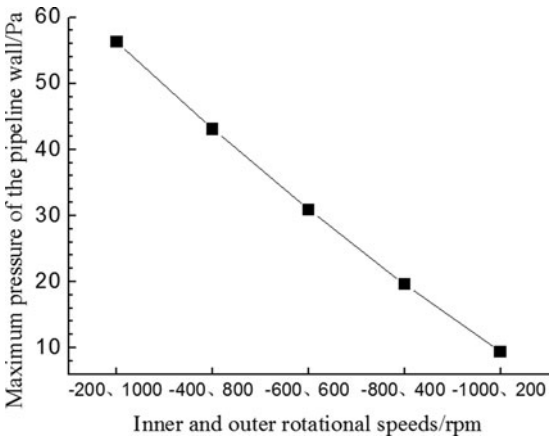


Fig. 23. Relation curve between maximum pressure of the pipeline wall and inner and outer rotational speed sum.

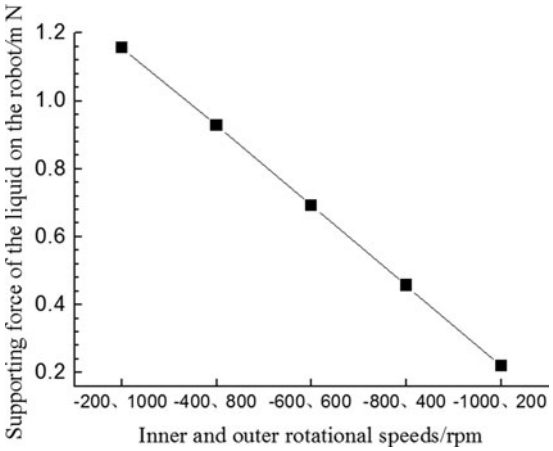


Fig. 24. Relation curve between supporting force of the liquid on the robot and inner and outer rotational speed sum.

increased, the robotic axial thrust force is negative, and its direction is opposite to that of the running speed, and the value is increased. This shows that in the process of operation, the resistance of liquid to the robot will be increased. When the robotic running speed is increased, the supporting force of the liquid is slightly decreased.

https://doi.org/10.1017/S0263574714001507 Published online by Cambridge University Press

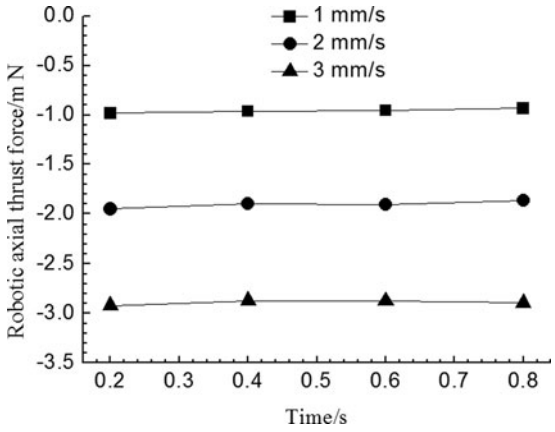


Fig. 25. Relation curve between robotic axial thrust force and robotic running speed.

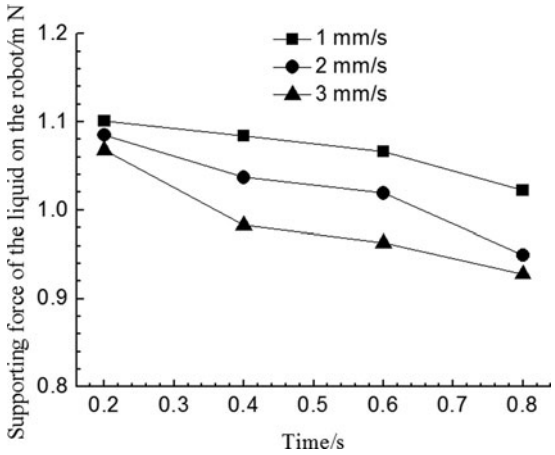


Fig. 26. Relation curve between supporting force of the liquid on the robot and robotic running speed.

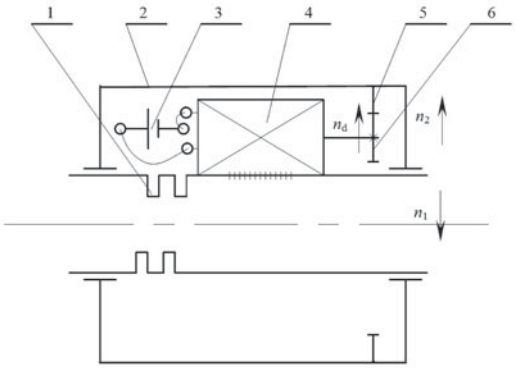
5. Experimental Verification of the Inner Spiral Robot

The robotic axial thrust force and the supporting force of the liquid on the robot of the proposed inner spiral robot in the liquid pipeline are analyzed by the numerical method. What is the actual operating situation in the liquid pipeline? Can the robot move forward and be suspended in a liquid environment? These problems are needed to be experimentally verified. Considering such problems as the manufacture of micro batteries, the manufacture of other micro components, and the assembly of the microrobot, an inner spiral driving device (that is the robotic prototype) is designed and fabricated according to the working principle of the inner spiral robot. Through the running experiment in the pipeline full of 201 methyl silicone oil, the rationality and feasibility of the proposed robot are verified.

When the inner spiral robot works in a small pipeline full of liquid, the robot is suspended in the pipeline by means of the wedge force produced by the liquid between the robotic shell and the pipeline wall, and it moves by the liquid reacting thrust force because of the high-speed rotation of the spiral inner shaft, so there are no relatively fixed parts in the rotating process. Therefore, according to the above working principle of the inner spiral robot, the designed inner spiral driving device adopts the epicyclic gear train, the structural principle is shown in Fig. 27. Taking into account the external power supply affecting the robotic operation and force, the battery is built-in.

As shown in Fig. 27, the micro motor 4 is fixed on the spiral inner body 1, and it is direct current motor with the diameter of 8 mm. The inner and outer bodies 1 and 2 are connected into a whole through a bearing. The reference circle diameter of the planetary wheel 6 (i.e. the gear on the micro motor output shaft) is d, and the planetary wheel is driven by the micro motor and is meshed with the sun wheel 5 (i.e. the smooth outer body), and the reference circle diameter of the sun wheel is D. The

https://doi.org/10.1017/S0263574714001507 Published online by Cambridge University Press



1-Spiral inner body 2-Smooth outer body 3-Battery 4-Micro motor
5-Sun wheel 6-Planetary wheel

Fig. 27. Structural principle of the designed inner spiral driving device.

planetary wheel and the sun wheel have the same modulus. The planetary wheel number of teeth is 12, and the sun wheel number of teeth is 192.

When the power is switched on, the rotational speed of the micro motor is n_d, and the rotational speed of the inner body is n_1, and the rotational speed of the outer body is n_2, so it is

$$\frac{n_2 - n_1}{n_d - n_1} = \frac{d}{D}. \tag{7}$$

When n_1 is 0, the maximum rotational speed of the outer body is

$$n_{2\max} = \frac{d}{D} n_d,$$

When n_2 is 0, the maximum rotational speed of the inner body is

$$n_{1\max} = -\frac{d}{D-d} n_d.$$

Negative sign indicates that the rotational directions of the inner body and outer body are opposite.

In the practical operation, the inner and outer surface rotational speeds n_1 and n_2 will reach the dynamic balance with the inner and outer loads varying, so as to drive the robot move at a constant speed.

Figure 28 is the prototype system of the inner spiral robot. Figure 29 is the exploded view of the robotic prototype, and the parts include the left spiral inner body with the lining, smooth outer body, covers, micro motors, no. 9 batteries, wireless transceiver module, and remote controller. The smooth outer body, spiral inner body, lining, and covers are made of aluminum alloy. The length of the prototype is 60 mm, the outer diameter is 50 mm, and the weight is 102 g. The inner spiral parameters are: inner diameter is 21 mm, thread number is 6, spiral groove is rectangular, groove face width is 1.5 mm, groove bottom width is 4.5 mm, groove depth is 2.5 mm, and spiral angle is 28.6°.

The experimental pipeline is a transparent organic glass pipeline, its diameter is 59 mm, and its length is 1200 mm. Experimental liquid is 201 methyl silicone oil, and its viscosity is 1 Pa s. Through the wireless remote switching on the micro motor power, the inner and outer surfaces rotate simultaneously, and the robot runs slowly in the oil, as shown in Fig. 30. Figures 31–33 are respectively the forward displacements of the robot in the pipeline at 0, 10, and 20 s. The measured forward average speed is 2 mm/s, and the measured backward average speed is 1.8 mm/s when the micro motor power is reversely switched on. It is feasible that this spiral in-pipe robot works in liquid environment.

https://doi.org/10.1017/S0263574714001507 Published online by Cambridge University Press

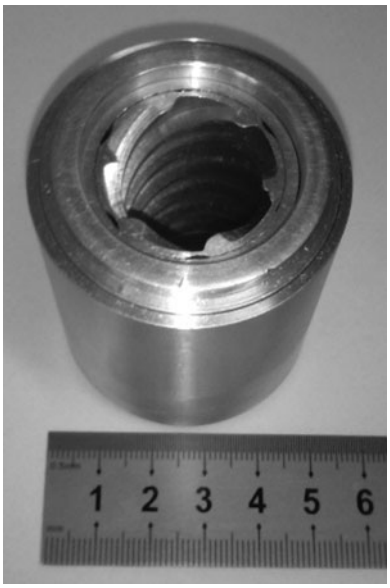


Fig. 28. Robotic prototype system.

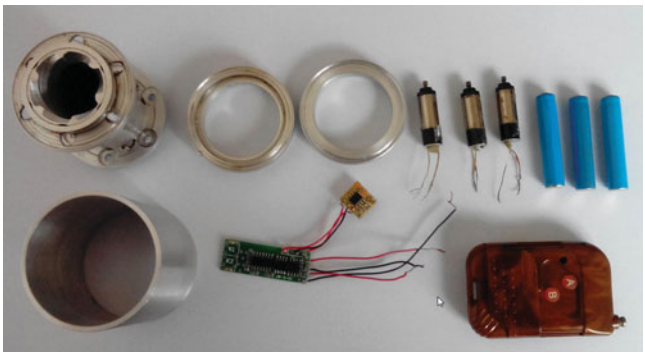


Fig. 29. The parts of the robotic prototype system.

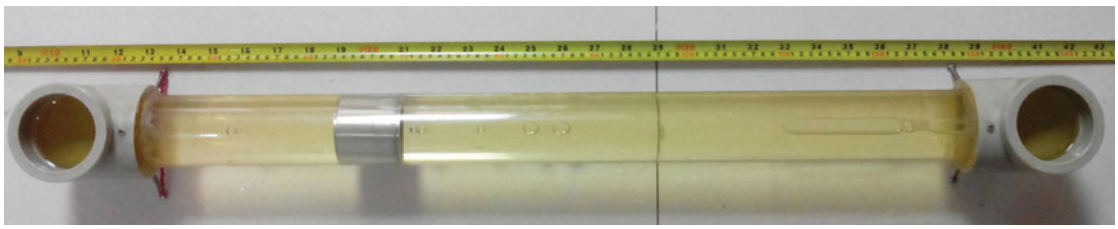


Fig. 30. The inner spiral robot in the pipeline filled with oil.

6. Structural Parameter Optimization of the Inner Spiral Robot

The above research shows that the inner spiral robotic axial thrust force is not large, so improving the robotic axial thrust force of this robot is a key consideration. Because the inner spiral robotic shell is a smooth surface, the robotic structural parameters influencing the robotic axial thrust force are the geometrical parameters of the inner spiral groove. The inner spiral structural parameters are shown in Fig. 34 and include: (1) parameter a_1 (groove root width), (2) parameter b_1 (groove face width), (3) dip angle α_1, (4) groove depth h_1, (5) spiral angle Φ_1, and (6) thread number n_1. In Fig. 34, t_1 represents inner spiral pitch, and Φ_1 equals $\arctan(n_1\ t_1/(\pi\ d_1))$, where d_1 is outer diameter of the inner spiral groove.

Considering the influences of the six inner spiral structural parameters on the robotic performance are not linear and are coupling each other, in order to find the optimal combination of the structural

https://doi.org/10.1017/S0263574714001507 Published online by Cambridge University Press

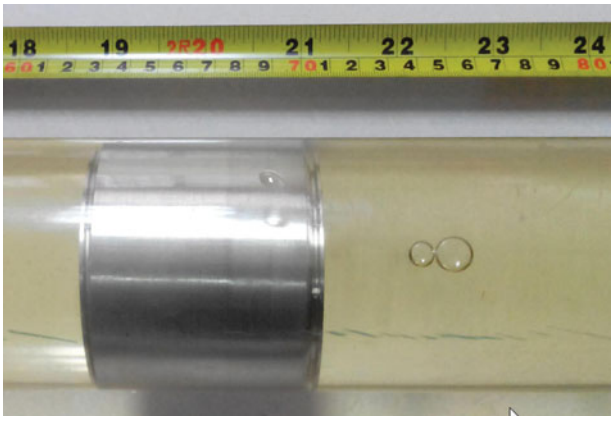


Fig. 31. The forward displacement of the robot in the pipeline at 0 s.

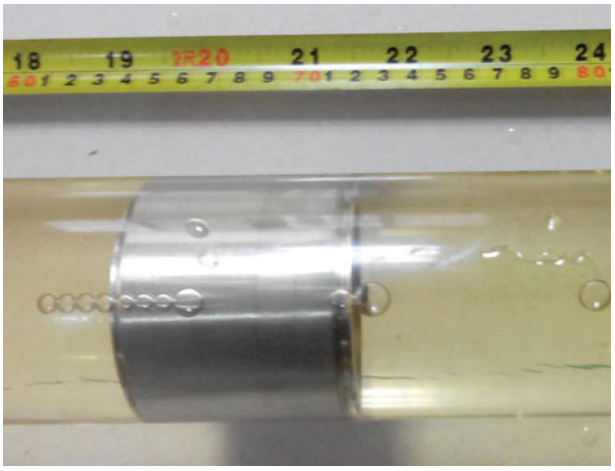


Fig. 32. The forward displacement of the robot in the pipeline at 10 s.

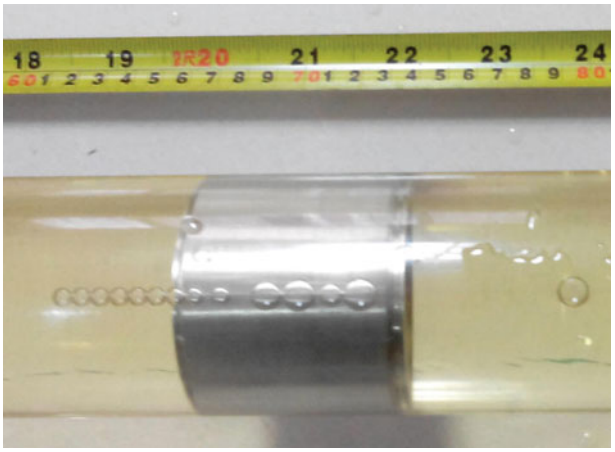


Fig. 33. The forward displacement of the robot in the pipeline at 20 s.

parameters of the maximal robotic axial thrust force, the orthogonal experimental optimization method is introduced.

For convenience, we use lead s_1 ($s_1 = n_1\ t_1$) as a substitute for spiral angle Φ_1 and set six inner spiral structural parameters as six experimental factors. Each parameter is given three different typical values to represent three experimental levels, and the experimental index is defined as the robotic

https://doi.org/10.1017/S0263574714001507 Published online by Cambridge University Press

Table I. Orthogonal experiment of inner spiral structural parameters of the inner spiral robot.

No.	a_1 (mm)	b_1 (mm)	α_1 (°)	h_1 (mm)	s_1 (mm)	n_1	Axial thrust force (m N)
1	0.5	0.75	70	0.2	10.54	6	0.031
2	0.5	0.75	90	1	12.57	10	0.029
3	0.75	0.5	90	0.2	15	8	0.096
4	0.75	1	110	0.6	10.54	6	0.008
5	1	0.5	110	0.6	12.57	10	0.004
6	1	1	70	1	15	8	0.040
7	0.5	0.5	110	1	15	6	0.079
8	0.5	1	110	0.2	12.57	8	0.015
9	0.75	0.5	70	1	12.57	10	0.112
10	0.75	0.75	70	0.6	10.54	8	0.017
11	1	0.75	90	0.6	15	6	0.053
12	1	1	90	0.2	10.54	10	0.018
13	***0.5***	***0.5***	***90***	***0.6***	***10.54***	***8***	***0.141***
14	0.5	1	70	0.6	15	10	0.004
15	0.75	0.75	110	0.2	15	10	0.022
16	0.75	1	90	1	12.57	6	0.044
17	1	0.5	70	0.2	12.57	6	0.039
18	1	0.75	110	1	10.54	8	0.027

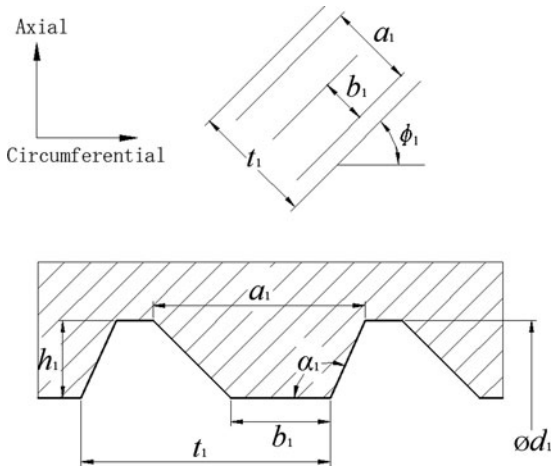


Fig. 34. Inner spiral structural parameters of the inner spiral robot.

axial thrust force. If the tests are done, 729 (3^6) tests are needed, and a set of the optimal structural parameters is found. According to ref. [20], using the orthogonal table $L_{18}(3^6)$ shown in Table I, we can obtain the optimal solution through only 18 tests.

According to the 18 sets of design parameters in Table I, every inner spiral robotic 3D system is respectively modeled and numerically calculated. From the results of Table I, the optimal inner spiral structural parametrical combination of the robotic optimal performance (i.e. the maximal robotic axial thrust force) is: parameter a_1 is 0.5 mm, parameter b_1 is 0.5 mm, dip angle α_1 is 90°, groove depth h_1 is 0.6 mm, lead s_1 is 10.54 mm, thread number n_1 is 8, and the value of the robotic maximal axial thrust force is 0.141 m N.

In order to let these inner spiral structural parameters be dimensionless, we define parameter β_{11} (the ratio of groove root width to pitch) as equal to a_1/t_1, parameter β_{12} (the ratio of groove face width to pitch) equal to b_1/t_1, and parameter γ_1 (the ratio of groove depth to outer diameter of inner spiral groove) equal to h_1/d_1. So the optimal inner spiral structural parametrical combination of the robotic maximal axial thrust force is: parameter β_{11} is 0.38, parameter β_{12} is 0.38, dip angle α_1 is 90°, parameter γ_1 is 0.15, spiral angle Φ_1 is 40°, and thread number n_1 is 8.

https://doi.org/10.1017/S0263574714001507 Published online by Cambridge University Press

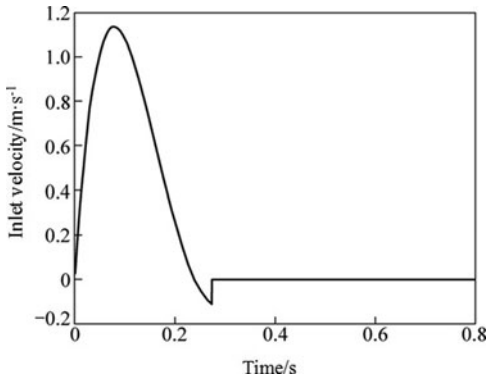


Fig. 35. Computed average blood flow velocity curve of aorta.

7. Performance Analysis of the Robot in Pulsating Flow

7.1. Pulsating blood flow function

For the sake of convenience, we assume that the working pipeline is blood vessel. Due to intermittent ventricular ejection of the heart, blood flow in the blood vessel is greatly pulsating. When it is at resting heart rate, blood flow is almost zero, and only in the ejection period, blood flow exists. The positive flowing time is about 1/4 to 1/3 of the heartbeat cycle.[21] Now we assume that the blood vessel is aortic, and its wall is simplified as rigid. Heart beat frequency is 75 times/min, that is, the heart cycle is 0.8 s. Among it, the shrinkage period accounts for 0.3 s, and the diastolic period accounts for 0.5 s. The computed average velocity curve of aorta is shown in Fig. 35, and the expression is given below:[21]

$$V_{\text{inlet}}(t) = \begin{cases} 2.4e^{-7.557t}\sin 13.09t & (0 \le t \le 0.24) \\ -0.343e^{-7.557(t-0.24)}\sin 13.09(t-0.24) & (0.24 < t \le 0.2743)\,, \\ 0 & (0.2743 < t \le 0.8) \end{cases} \tag{8}$$

where V_{inlet} is the computed average velocity of aorta, and the unit is m/s; t is time, and the unit is s.

7.2. Numerical calculation of the robotic system

According to the actual situation of the human body, we assume that density of blood is 1053.1 kg/m^3, dynamic viscosity of blood is 0.0045135 Pa s, and the direction of blood gravity is the negative direction of y axis. The rotational speed of the robotic shell is 600 r/min, the rotational speed of the robotic inner shaft is –600 r/min, and the numerical method and other parameters are consistent with the above static flow.

Figures 36 and 37 are respectively the curves of the robotic axial thrust force and the maximum pressure of the vascular wall in a pulsating cycle (0.8 s) when the robotic linear velocity changes from 0 mm/s to 25 mm/s. As seen here, the changing trends of the robotic axial thrust force and the maximum pressure of the vascular wall are basically the same with the changing trend of the blood flow velocity, and the pressure of the vascular wall is within an acceptable range of people. When the high-speed rotating robot does not have running speed, the robotic axial thrust force is greater than the value when the robot runs. When the robot runs, the increasing liquid resistance decreases the robotic axial thrust force, and the maximum pressure of the vascular wall will be slightly higher than the value when the robot has no running speed. Contrasting the curves of the robotic axial thrust force and the maximum pressure of the vascular wall at different running speeds, the influence of the robotic running speed on the robotic axial thrust force and the maximum pressure of the vascular wall is not large.

https://doi.org/10.1017/S0263574714001507 Published online by Cambridge University Press

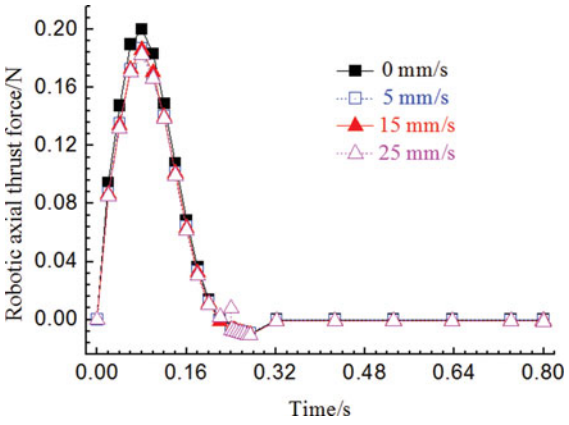


Fig. 36. Axial thrust force of the robot in a pulsating cycle.

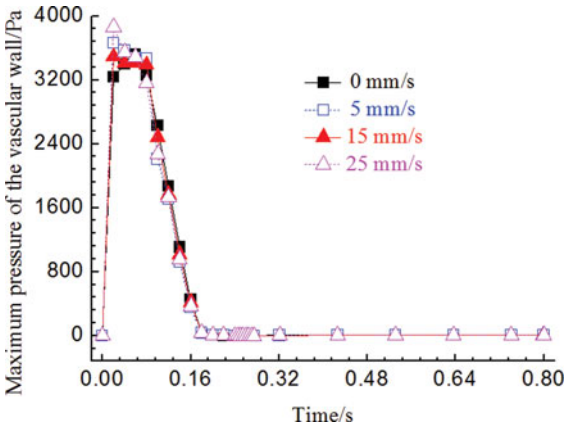


Fig. 37. Maximum pressure of the vascular wall in a pulsating cycle.

8. Conclusions and Future Work

A micro in-pipe robot using an internally threaded profile for propulsion is proposed, which is expected to be applied to intestinal tract, blood vessels, and other tiny pipelines filled with liquid in human body.

The dynamic model of the robot in the turbulent liquid pipeline is established, and the correctness of the adopted numerical method is verified. The CFD method is used to solve the flow filed, and the influences of environmental parameters (liquid density, liquid viscosity, pipeline diameter, and eccentricity) and operating parameters (inner spiral rotational speed, outer surface rotational speed, inner and outer surface rotational speed sum, robotic running speed) on the robotic performance (the axial thrust force, the maximum pressure of the pipeline wall, and the supporting force of the liquid on the robot) are obtained. The axial thrust force of the inner spiral robot is proportional to liquid density, liquid viscosity, eccentricity, and outer surface rotational speed, and it is inversely proportional to pipeline diameter, inner spiral rotational speed, and robotic running speed. The maximum pressure of the pipeline wall is proportional to liquid density, liquid viscosity, eccentricity, and outer surface rotational speed, and it is inversely proportional to pipeline diameter, and it has little relation with inner spiral rotational speed. The supporting force of the liquid on the robot is proportional to liquid viscosity, eccentricity, and outer surface rotational speed, and it is inversely proportional to liquid density, pipeline diameter, and robotic running speed, and it has little relation with inner spiral rotational speed.

According to the working principle of the inner spiral robot, an inner spiral driving device is designed and fabricated. Through the running experiment in the pipeline full of a certain viscous liquid, the feasibility of the proposed robot is verified.

https://doi.org/10.1017/S0263574714001507 Published online by Cambridge University Press

By orthogonal experimental optimization method, the optimal inner spiral structural parametrical combination of the robotic maximal axial thrust force is: parameter β_{11} is 0.38, parameter β_{12} is 0.38, dip angle α_1 is 90°, parameter γ_1 is 0.15, spiral angle Φ_1 is 40°, and thread number n_1 is 8.

Adopting the pulsating blood flow function as the inlet condition, in a pulsating cycle, the robotic axial thrust force and the maximum pressure of the vascular wall are numerically calculated. The changing trends of the robotic axial thrust force and the maximum pressure of the vascular wall are basically the same with the changing trend of the blood flow velocity, and the pressure of the vascular wall is within an acceptable range of people. The influences of the robotic running speed on the robotic axial thrust force and the maximum pressure of the vascular wall are not large. When the high-speed rotating robot does not have running speed, the robotic axial thrust force is greater than the value when the robot runs, and the maximum pressure of the vascular wall will be slightly less than the value when the robot runs.

The proposed inner spiral robot uses micro batteries for energy supply, so the development of the battery for large capacity and small size is an important foundation of this robot for long working hours. Another way of energy supply is external magnetic drive.

The size of the robotic prototype is bigger than that of practical requirements, such as human blood vessels, so it should be further miniaturized. The *in vivo* experiments of the inner and outer spiral robot have not been done in the organismal lumen, and the real clinical application is still a long distance. A lot of experimental research is also required.

Acknowledgements

This work was supported in part by the Construct Program of the Key Discipline in Hunan province and in part by the Scientific Research Fund of Hunan Provincial Education Department under grant 13B141 and in part by the National Natural Science Foundation of China under grants 71271215, 71221061, and 51075209 and in part by the 863 National High Technology Research and Development Plan Projects under grant 2013AA041004. It was also supported in part by the Hunan Provincial Natural Science Foundation under grant 13JJ6082 and in part by the Science and Technology Plan Projects of Jiangsu Province under grants BK2012798, BY2012011 and BK 2013003-10 and in part by the Scientific Research Projects of Shanghai under grant 124119a3900.

References

1. G. D. Meron, "The development of the swallowable video-capsule (M2A)," *Gastrointest. Endosc.* **52**(6), 812–819 (2000).
2. RF System Lab. (2014). Sayaka. Available at: http://www.rfsystemlab.com/en/sayaka/.
3. H. J. Park, H. W. Nam, B. S. Song, J. L. Choi, H. C. Choi, J. C. Park, M. N. Kim, J. T. Lee and J. H. Cho, "Design of Bi-Directional and Multi-Channel Miniaturized Telemetry Module for Wireless Endoscopy," *Proceedings of the 2nd Annual International IEEE-EMB Special Topic Conference on Microtechnologies in Medicine & Biology*, Madison, USA (May 2–4, 2002) pp. 273–276.
4. S. Maqbool, H. P. Parkman and F. K. Friedenberg, "Wireless capsule motility: Comparison of the Smartpill GI monitoring with scintigraphy for measuring whole gut transit," *Digestive Dis. Sci.* **54**(10), 2167–2174 (Aug. 2009).
5. S. Yim and M. Sitti, "Shape-programmable soft capsule robots for semi-implantable drug delivery," *IEEE Trans. Robot.* **28**(5), 1198–1202 (Oct. 2012).
6. M. Simi, P. Valdastri, C. Quaglia and P. Dario, "Design, fabrication and testing of a capsule with hybrid locomotion for gastrointestinal tract exploration," *IEEE/ASME Trans. Mechatronics* **15**(2), 170–180 (Apr. 2010).
7. Y. Nakazato, Y. Sonobe and S. Toyama, "Development of an in-pipe micro mobile robot using peristalsis motion," *J. Mech. Sci. Technol.* **24**(1), 51–54 (Jan. 2010).
8. L. Phee, A. Menciassi, D. Accoto, C. Stefanini and P. Dario, "Analysis of robotic locomotion devices for the gastrointestinal tract," *Springer Tracts Adv. Robot.* **6**, 467–483 (2003).
9. B. Kim, S. Lee, J. H. Park and J.-O. Park, "Design and fabrication of a locomotive mechanism for capsule-type endoscopes using shape memory alloys (SMAs)," *IEEE/ASME Trans. Mehatronics* **10**(1), 77–86 (Feb. 2005).
10. G. Yan, Q. Lu, G. Ding and D. Yan, "The Prototype of a Piezoelectric Medical Microrobot," *Proceedings of the International Symposium on Micromechatronics and Human Science*, Nagoya, Japan (Oct. 23, 2002) pp. 73–77.
11. M. S. Triantafyllou and G. S. Triantafyllou, "An efficient swimming machine," *Sci. Am.* **272**(3), 64–70 (Mar. 1995).

https://doi.org/10.1017/S0263574714001507 Published online by Cambridge University Press

12. L. Shi, S. Guo and K. Asaka, "A Novel Jellyfish-Like Biomimetic Microrobot," *Proceedings of the IEEE/ICME International Conference on Complex Medical Engineering*, Gold Coast, Australia (Jul. 13–15, 2010) pp. 277–281.
13. B. Chen, Y. Liu, S. Chen, S. Jiang and H. Wu, "A biomimetic spermatozoa propulsion method for interventional micro robot," *J. Bionic Eng.* **5**, 106–112 (Sep. 2008).
14. D. Byun, J. Choi, K. Cha, J. Park and S. Park, "Swimming microrobot actuated by two pairs of Helmholtz coils system," *Mechatronics* **21**(1), 357–364 (Feb. 2011).
15. K. Ikeuchi, K. Yoshinaka and N. Tomita, "Low invasive propulsion of medical devices by traction using mucus," *Wear* **209**(1–2), 179–183 (Aug. 1997).
16. C. Hu, D. Chen, M. Meng, L. Wang, H. Dai and W. Yang, "A Wireless Actuation System for Micro-Robot Moving Inside Pipeline," *Proceedings of the IEEE/ASME International Conference on Advanced Intelligent Mechatronics*, Xi'an, China (Jul. 2–5, 2008) pp. 653–658.
17. Y. Zhou, L. Li and D. Zhao, "New kind of micro-robot," *Chinese J. Mech. Eng.* **37**(1), 11–13 (Jan. 2001).
18. F. Wang, *Computational Fluid Dynamics Analysis—CFD Software Theory and Application* (Tsinghua University Press, Beijing, China, 2004) pp.113–123.
19. B. Chen, Study on the Endoscopic Micro Robots Operating in Liquid Environment, *Ph.D. Dissertation* (Hangzhou, China: Department of Mechanical Engineering, Zhejiang University, 2005).
20. K. Fang and C. Ma, *Orthogonal and Uniform Experimental Design* (Science Press, Beijing, China, 2001) pp. 239.
21. L. Qiu, Numerical Simulation and Experimental Study for Vascular Interventional Treatment by Bifurcated Artery, *Ph.D. Dissertation* (Chengdu, China: Department of Biomedical Engineering, Sichuan University, 2004).

https://doi.org/10.1017/S0263574714001507 Published online by Cambridge University Press